Geomechanics and Engineering, *Vol. 31, No. 4 (2022) 395-407*
https://doi.org/10.12989/gae.2022.31.4.395

Numerical study of rock mechanical and fracture property based on CT images

Nan Xiao[a], Li-Cheng Luo[b], Fu Huang* and Tong-Hua Ling[c]

School of Civil Engineering, Changsha University of Science and Technology, Changsha 410004, Hunan, China

(*Received July 4, 2022, Revised October 25, 2022, Accepted November 14, 2022*)

Abstract. In this paper, cracks with different angles are prefabricated in rock specimens to study the fracture characteristics of rock based on CT images. The rock specimens are prepared for compression tests according to the standard recommended by ISRM (International Society for Rock Mechanics). The effects of different angles on rock mechanical properties and crack propagation fracture modes are analyzed. Then, based on the cohesive element method and CT images, the relationship between porosity and Young's modulus as well as the fracture property is explored by the numerical modelling. In the modelling, the distribution of Young's modulus is determined by the CT image through the field variable method. The results show that prefabricated cracks reduce the mechanical properties of rock. The closer the angles of the prefabricated crack is, the greater the Young 's modulus of the rock sample is. The failure process of each specimen with prefabricated cracks is formed by the initiation and propagation of crack, and the angle of the prefabricated crack will affect the type of extended crack. As part of the numerical model proposed in this paper, the microstructure of rocks is reflected by CT images. The numerical results verify the effectiveness of the cohesive element method in the study of crack propagation for rock. The rock model in this paper can be used to predict engineering disasters such as collapse and landslide caused by rock fracture, which means that the methodology adopted in this paper is comprehensive and important to solve rock engineering problems.

Keywords: cohesive element method; CT; field variables method; fracture; rock

1. Introduction

Discontinuous structures such as cracks and joints significantly affect the mechanical properties of rock, making it different from other media. The connection of these discontinuous structures will lead to the formation of a weak structural plane in the rock mass. The rock mass will slide along the weak structural plane under natural disturbances such as rainfall, earthquake, or artificial disturbances such as construction, which causes various engineering disasters and threatens the safety of human beings. Therefore, the influence of various cracks and joints on the mechanical performance of rock is an important issue in the field of rock mechanics and engineering.

Since the last century, many extensive and in-depth research projects have been conducted on rocks to understand how the discontinuous structure affects the mechanical properties of rock. Xie *et al.* (2016) quantitatively analyzed the effect of crack surface friction on the initiation and propagation of closed cracks. In this research, when the inclination angle is constant, the shear stress of the crack surface increases with the increase of the friction coefficient, when the friction coefficient is constant, the shear stress of the crack surface decreases with the increase of the inclination angle. Lee and Jeon (2011) conducted uniaxial compression tests on three different types of specimens of PMMA (polymethyl methacrylate), gypsum type, and Huangdeng granite. Yang *et al.* (2018) studied the effect of elliptical crack angle on the strength and deformation behavior of sandstone specimens under uniaxial compression, and the strength, Young's modulus and peak strain of the defective specimens are all lower than those of the intact specimen, and the Young's modulus decreases first and then increases with the increase of the elliptical crack angle. Although the works mentioned above have concentrated on the crack propagation mode for rocks with pre-existing cracks, the influence of the angle of the pre-existing crack on rock failure has not been noticed based on the CT images yet.

Numerical modelling have become a powerful tool to study rock failure in recent years. Numerical modelling methods are low-cost and high-efficiency, including Finite Element (FEM) (Pradhan and Siddique 2020, Li and Wong 2012), Discrete Element (DEM) (Fakhimi and Alavi Gharahbagh 2011, Scholtès and Donzé 2012), Boundary Element (BEM) (Leonel and Venturini 2011, Lo Cascio *et al.* 2021) and others, which is widely used in the field of geotechnical engineering. The problem of static cracks can be solved by these methods, but these methods are not ideal for the problem of dynamic cracks. The traditional FEM method, which is the most popular and mature, is difficult

*Corresponding author, Professor
E-mail: hfcsust@csust.edu.cn
[a]Lecturer
E-mail: xn@csust.edu.cn
[b]Master Student
E-mail: 490873464@qq.com
[c]Professor
E-mail: lingtonghua@163.com

ISSN: 2005-307X (Print), 2092-6219 (Online)

in dealing with crack propagation problems in rocks. As a new method based on FEM, the cohesive element method assumes the existence of stress at the interface and is able to simulate the mechanical state in the bonding area. To simulate the complex fracture process of rocks, the traction-separation criterion becomes effective in the viscous zone, which represents a thin layer with minimal geometric thickness. And the cohesive element can be embedded on the surface of the solid element in the program based on the cohesive element method. This method keeps a relatively clear relationship between the elements in the finite element grid, avoids repeated searches for data, improves efficiency, and reduces insertion difficulty. In general, this new numerical simulation method has a good performance in solving crack propagation problems for rock, which can help us to improve the understanding the process of rock failure.

Engineering activities, such as underground space development, tunnel excavation, and dam construction, have always been closely related to rock mass. Engineering disasters are also caused by the failure of the rock mass, which is dependent on the formation of weak structural planes by the expansion of cracks in the rock. It has positive meaning for engineering construction and disaster prevention to reasonably consider the diversity of spatial distribution of the joints and the mesoscopic internal structure of rocks, so as to study the failure mechanism of rock mass under relevant conditions. Liu *et al.* (2022) adopted an experimental system to study the distribution evolution process of tunnel excavation and earth pressure. Wu *et al.* (2019) studied the mechanical properties of yieldable steel ribs supporting roadways in rheological rocks. Hong *et al.* (2020) quantitatively analyzed the complex interaction behavior of piles, tunnels and surrounding soil and rock.

In this paper, first, a standard sandstone cylinder specimen of 50 mm×50 mm×100 mm is scanned by a CT machine to obtain the spatial information of the internal microstructure. Then, compression tests are carried out on intact specimens and pre-cracked specimens with different angles. After, the relationship between porosity and Young's modulus is studied based on our previous work. Finally, based on the CT data, a numerical model with different Young's modulus in spatial position is established by the field variables method, and the cohesive element method is used to model the crack propagation process. The strength, deformation, and failure characteristics of rock are studied considering the diverse spatial location of pre-cracks. Through the appropriate comprehensive consideration of complex environmental and geological conditions, the method of this paper can be used to simulate the deformation and failure of rock mass, and to predict the engineering disasters caused by rock fracture, such as collapse, landslide, and deep rockburst caused by rapid crack propagation. As a combination of convenience and flexibility, the method is highly useful for solving rock engineering problems in a comprehensive and significant way.

2. Methodology

The PFC (Particle Flow Code) is the most widely used code based on the discrete element method (DEM). It studies the mechanical properties of the medium from the perspective of microstructure. The macroscopic mechanical properties of the medium depend on the geometric and mechanical properties of the particles and the bond. The discrete element method is based on empirical calculation. The motion, stress and deformation of the object are simplified, so that the stress system in the calculation cannot be completely balanced. And the calculation accuracy of the stress distribution or strain distribution inside the element is lower than that of the finite element method (FEM). The cohesive element method in Abaqus characterize the deformation of the material based on the finite element method, and the initiation, propagation, penetration of the cracks and the contact interaction after failure are all described by the discretization. Thus the cohesive element method in Abaqus can achieve the accurate description of the material failure. The cohesive element method is used to simulate the debonding process of interface. By analyzing the constitutive relation, the cohesion element method is similar to the virtual crack method. The cohesive element method is an intelligent and efficient method, and is also used to simulate the fracture process of brittle materials such as rock and concrete (Jiang and Meng 2018, Wu *et al.* 2018, Nguyen *et al.* 2017, Pan *et al.* 2021, Unger *et al.* 2007, Hoover and Bažant 2014, Song *et al.* 2006). Based on traction-separation, the cohesive element method can be used to simulate crack propagation along a predetermined path or any other path. Crack path and crack propagation velocity become the natural results of this method. The cohesive element and the matrix element have the mesh topology, but the constitutive relationship is independent of each other. This characteristic determines that the cohesive element method is naturally suitable for the finite element analysis framework, and the cohesive constitutive model is especially suitable for studying complex fracture failure problems. Therefore, this paper uses the cohesive element as the basic element of the crack to model the fracture.

2.1 Theory adopted for cohesive element method

The cohesive element method used in this paper is based on the bonding crack model proposed by Dugdale (1960) and Barenblatt (1962). The virtual crack model proposed by Hillerborg *et al.* (1976), assumes that the cohesive element has stress at the interface, and can be used to model the mechanical behavior in the bonding area. The single layer of cohesive elements in the thickness direction acts as an adhesive zone. The viscous zone represents a thin layer of minimal geometric thickness, acting as the fracture region of the rock. The elastic stage, damage, and cracking criteria of the cohesive element method will be introduced in the following.

In the initial stage before the damage of cohesive element, the stress-strain satisfies the following linear elastic relationship

$$t=\begin{Bmatrix} t_n \\ t_s \\ t_t \end{Bmatrix}=K\varepsilon=\begin{bmatrix} K_{nn} & K_{ns} & K_{nt} \\ K_{ns} & K_{ss} & K_{st} \\ K_{nt} & K_{st} & K_{tt} \end{bmatrix}\begin{Bmatrix} \varepsilon_n \\ \varepsilon_s \\ \varepsilon_t \end{Bmatrix} \quad (1)$$

where t is the traction stress vector, which consists of three components, namely, the normal stress t_n, the tangential stress t_s, and t_t. K is the element stiffness matrix, K_{nn} is the initial normal stiffness, K_{ss} and K_{tt} are the initial tangential stiffness. The matrix represents the relationship between displacement and stress in different directions. The distance between the two crack surfaces is zero before crack initiation, therefore the values of K_{nn}, K_{ss} and K_{tt} are generally infinite numbers, which will cause difficulty in the convergence of the simulation calculation. In the cohesive element method, the appropriate initial stiffness will be intelligently selected to ensure smooth convergence of the calculation of the stress state. ε is the strain vector, which also consists of three components, namely the normal strain ε_n, tangential strain ε_s, and ε_t. The strain can be defined as follows

$$\varepsilon_n=\frac{d_n}{T_0},\varepsilon_s=\frac{d_s}{T_0},\varepsilon_t=\frac{d_t}{T_0} \quad (2)$$

where d_n is the normal displacement, d_s and d_t are the tangential displacements. The thickness of the cohesive element is zero, in which case the calculation of the strain will produce singularities. To avoid singularity, the constitutive thickness T_0=1 can be used instead of the actual thickness to calculate the stress and strain of the cohesive element, so that the strain and displacement of the cohesive elements are numerically equal to each other. The appropriate initial stiffness and the replacement of the actual thickness with the constitutive thickness indicate that the cohesive element method is able to avoid some potential problems through self-adaptation and parameter selection, which is an intelligent and reliable method for the study of rock fracture.

After the linear elastic stage, the damage to cohesive elements begins. The damage depends on the damage evolution law. Once the damage initiation criterion is satisfied, the damage will occur according to the damage evolution law. The cohesive crack model mentioned in the previous section assumes that there are normal traction force t_n and tangential traction forces t_s, t_t on the crack surface. Considering the inhomogeneity of microstructure in rock, the fracture of rock should be mixed-mode that combine tangential and tangential components (Zhou *et al.* 2016, Galindo *et al.* 2021). The schematic diagram of the viscous traction separation response of the mixed-mode is shown in Fig. 1. t_{no}, t_{so}, t_{to}, and t_{mo} represent pure normal traction force, pure shear traction force, pure shear traction force, and effective traction force at the beginning of the damage, respectively. d_{no}, d_{do}, d_{to}, and d_{mo} represent the pure normal displacement, pure shear displacement, pure shear displacement, and effective displacement respectively, at the beginning of the damage. d_{nf}, d_{sf}, d_{tf}, and d_{mf} represent pure normal displacement, pure shear displacement, pure shear displacement, and effective displacement, respectively when the element completely fails. The relationship between T (which means Traction) and S (which means separation) is linear in Fig. 1. The area enclosed by the curve represents the opening-type (I-type) fracture energy G_{IC} and the sliding-opening (II-type) fracture energy G_{IIC}, respectively in Fig. 1.

At the damage evolution stage, the stiffness of the cohesive element degrades. To describe the degree of damage, a damage variable index D is adopted in this paper, and it evolves from 0 to 1 as the damage accumulates. The function of the effective relative displacement d_m is defined as follows

$$d_m=\sqrt{\langle d_n\rangle^2+d_s^2+d_t^2} \quad (3)$$

$\langle\ \rangle$ is the Macaulay bracket. When $d_n \geq 0$ (tension), $\langle d_n\rangle = d_n$, when $d_n<0$ (compression), $\langle d_n\rangle=0$. Macaulay bracket is used to indicate the pure compressive deformation or stress state which does not cause damage. For the linear softening criterion of the mixed-mode cohesive traction separation response in Fig. 1, the damage variable index D can be written as

$$D=\frac{d_{mf}\left(d_{mm}-d_{mo}\right)}{d_{mm}\left(d_{mf}-d_{mo}\right)} \quad (4)$$

where d_{mm} is the maximum effective displacement. With the damage variable index D, the corresponding stress component can be expressed as

$$\begin{cases} t_n=\begin{cases}(1-D)t_{no}, t_{no}\geq 0 \\ t_{no} \quad\quad ,t_{no}<0\end{cases} \\ t_s=(1-D)t_{so} \\ t_t=(1-D)t_{to}\end{cases} \quad (5)$$

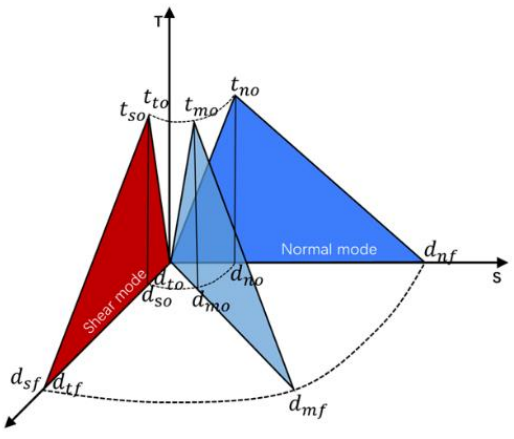

Fig. 1 Cohesive traction separation response of mixed-mode

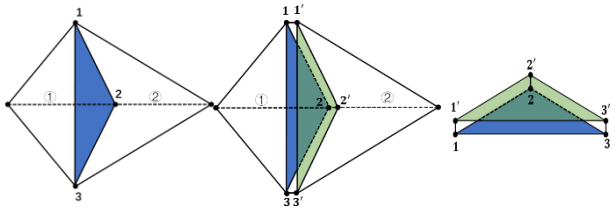

(a) Two adjacent finite elements (b) Insert a 3D cohesive element (c) A zero-thickness cohesive

Fig. 2 Inserting a cohesive element into a finite element

The degraded stiffness K_n, K_s, K_t can also be expressed by D with the initial stiffness K_{nn}, K_{ss}, K_{tt} as

$$\begin{cases} K_n = (1-D)K_{nn} \\ K_s = (1-D)K_{ss} \\ K_t = (1-D)K_{tt} \end{cases} \tag{6}$$

The damage evolution of the rock can be regarded as the crack propagation based on the cohesive element method. The damage model consists of three parts: the criterion of crack initiation, the criterion of damage evolution, and the post-processing of element failure. In this paper, the criterion of quadratic nominal stress is applied to crack initiation. This criterion assumes that crack initiation occurs when the value of the quadratic interaction function involving the normal stress ratio reaches 1, which is expressed as follows

$$\left\{\frac{\langle t_n \rangle}{t_{no}}\right\}^2 + \left\{\frac{t_s}{t_{so}}\right\}^2 + \left\{\frac{t_t}{t_{to}}\right\}^2 = 1 \tag{7}$$

2.2 Method adopted for embedded cohesive element

Embedding cohesive element in the mesh presents certain challenges for the intricate topological relationship in three-dimensional (3D) space. Therefore, the same finite elements should be selected during meshing. To achieve the crack propagation path and to model the fracture process, the tetrahedral finite element should be preferentially selected in the initial finite element mesh. In addition, the cohesive elements that constitute the crack are inserted between two adjacent finite elements. The numerical rock model is meshed at first to obtain the node coordinate information about the finite element, and then the cohesive element is inserted into the model. The method of embedding tetrahedral finite elements with 3D cohesive elements can be illustrated in Figs. 2(a)-2(c). Fig. 2(a) shows two adjacent tetrahedral finite elements sharing three nodes. A node shared by adjacent elements is called a parent node, and then the parent node will be replaced by a new node with the same coordinates which is called a child node. The child nodes of each tetrahedral finite element will be connected to obtain a triangular face, as shown in Fig. 2(b). Finally, the superposition of two adjacent independent triangular faces leads to the formation of a 3D cohesive element as shown in Fig. 2(c) (Su *et al.* (a) 2010, Su *et al.* (b) 2010, Jiang and Meng 2018). It should be noted that the thickness of the inserted cohesive element is zero, the thickness is shown in the figure only to indicate position. In addition, due to a large number of finite elements, it is difficult to manually insert cohesive elements between finite elements. Therefore, a compiled plug-in is used to insert cohesive elements between finite elements. The steps of the embedding method can be briefly described as follows:

(1) Create three different databases to store the information of nodes, elements, and surfaces in the initial finite element mesh.

(2) Create another database to store the information of the node and element after disassembly.

(3) After the finite element is split, the original element node changes, and the node number and other information about the finite element need to be updated.

(4) Embed the cohesive element in the element surface of the initial mesh to generate the cohesive element serial number and a node edge number.

(5) Generate a new input file in Abaqus

3. Mechanical and CT test results

In this paper, the rock samples are collected from Luoquan Town, Zizhong County, Sichuan Province. Sichuan is one of the three major sandstone-producing areas in China. Luoquan Town is located in the central Sichuan Basin, the middle reaches of the Tuojiang River. The landform is mainly hilly, with limestone reserves of 500 million tons, and coal reserves of 100 million tons. The sandstone in this area is characterized by fine particles, which belongs to white sandstone. The sand particle size of the rock sample is between 0.5-2 mm. 9 standard cylindrical specimens in size of 50 mm×50 mm×100 mm are prepared for the experiment from the rock samples. The standard for the rock sample and experiments conducted in this research is in accordance with ISRM suggested method (Altindag and Güney 2006). The diameters of the pilot hole in the center of the two pre-existing cracks are 1mm. The size of the pre-existing cracks is 10 mm in length and 0.4 mm in width which runs through the cylinder sample. The distance between the center of the hole and the end surface is 35

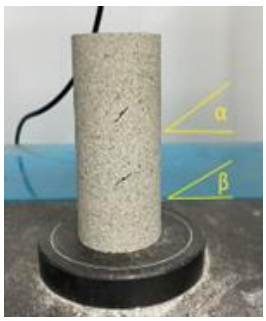

Fig. 3 Angles of pre-existing cracks in the specimen

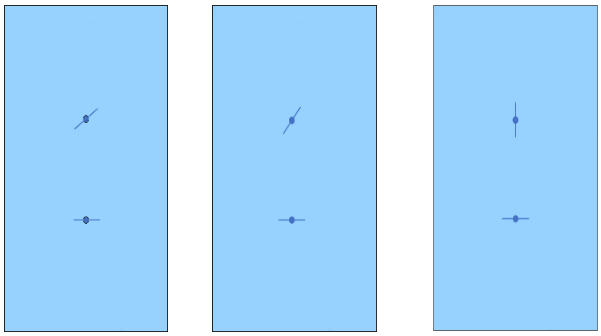

(a) No.1 (b) No.2 (c) No.3

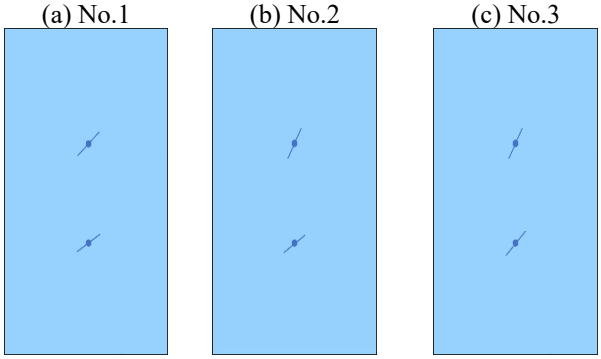

(d) No.4 (e) No.5 (f) No.6

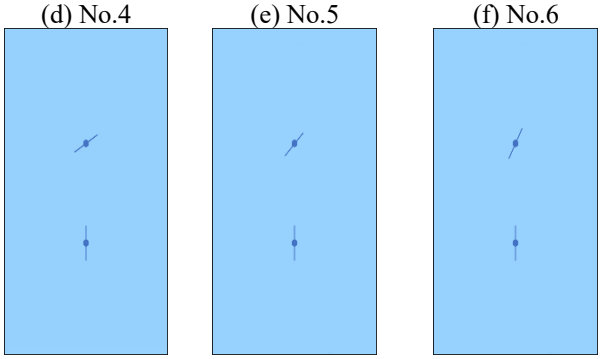

(g) No.7 (h) No.8 (i) No.9

Fig. 4 Schematic diagram of the pre-existing cracks in specimens

mm, and the distance between the two centers of the holes is 30 mm. The length of the prefabricated crack is set for the overall size of the specimen, which avoids the excessive influence of the crack length on the rock performance. Let α be the angle of the one pre-existing crack, and β represents the angle of the other one, as shown in Fig. 3.

The angles of the pre-existing cracks in specimens are arranged as shown in Fig. 4. The arrangement of the position of cracks is to study the influence of different angles on the crack propagation of the specimen. The detail about the angles can be found in Table 2.

The sandstone specimen was scanned by the CT machine, whose mode number is dxr-5001, as shown in Fig. 5. The detailed parameters of the CT machine are shown in Table1. The CT machine penetrates rocks by X-rays. During the penetration process, some X-ray photons are absorbed by the specimen, and the remaining photons pass through the specimen and are received by the detector. Then, the received X-ray photons are converted into electrical signals. The higher the density of the rock is, the stronger the absorption of X-ray photons is, and the less the X-ray photons received by the detector are. With the electrical signals, The scanning data can be obtained by computer processing. Figs. 6(a)-6(c) show the CT data obtained from the end and the middle section of the specimens. The mineral composition of the rock sample is identified by X-ray Diffraction analysis. The dominant minerals are quartz (α-SiO_2, accounting for 69.13%) and kaolin (Al_2O_3•$2SiO_2$•$2H_2O$, accounting for 24.9%). In addition, the rock sample also contains a small amount of Fe_2O_3 (accounting for 1.73%) and $CaCO_3$ (accounting for 1.73%) and some impurities. Compression tests are performed on the specimens by a computer-controlled rock tensile splitting machine whose mode number is YDW-100, as

Fig. 5 The CT machine

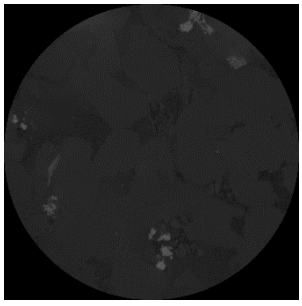

(a) One end section of the specimen

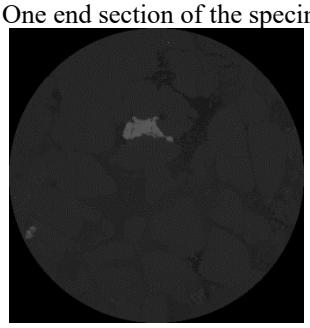

(b) The middle section of the specimen

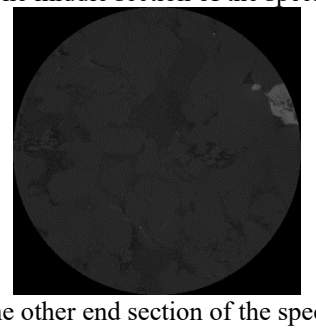

(c) The other end section of the specimen

Fig. 6 Two dimensional gray CT image

Fig. 7 Computer-controlled rock tensile splitting testing machine

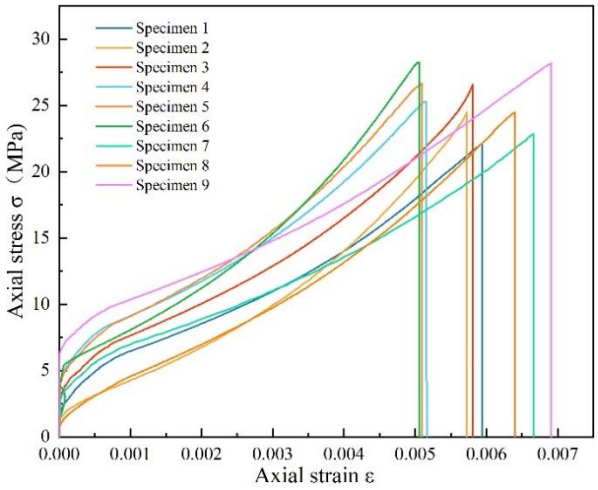

Fig. 8 Stress-strain curve of pre-cracked specimens

Table 1 Parameters of the CT scanner

Magnification	Voxel size (μm)	Image width (pixel)	Image height (pixel)	Voltage (kV)	Current (μA)
90	1.1070	3052	2400	120	110

shown in Fig. 7. The loading mode is displacement, the loading rate is set to 2 mm/min, and the data are recorded in real-time. In the experiment, the data of strain are collected at a frequency of 50 times/second. The experimental data of the rock specimen are listed in Table 2, and the stress-strain curves of the specimens with pre- existing cracks are shown in Fig. 8.

4. Analysis of mechanical properties

4.1 Strength characteristics of specimens

The rock specimens are divided into three groups according to their angles. Nos.1-3 specimens belong to the 1st group, Nos.4-6 specimens belong to the 2nd group and Nos.7-9 specimens belong to the 3rd group. The stress-strain curves of the specimens are shown in Figs. 9(a)-9(c).

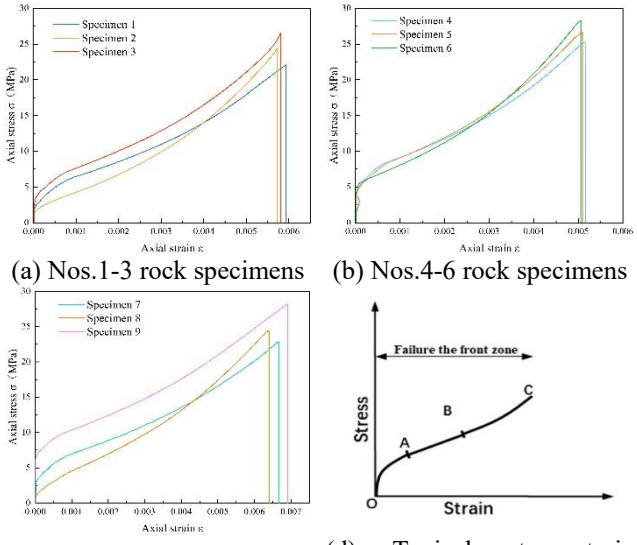

(a) Nos.1-3 rock specimens (b) Nos.4-6 rock specimens

(c) Nos.7-9 rock specimens (d) Typical stress-strain curve before failure

Fig. 9 Stress-strain curve diagram

The peak values of the axial strain for the specimens are inconsistent. The stress-strain curve before the peak can be divided into three stages, namely, OA, AB, and BC as shown in Fig. 9(d). The characteristics of each stage can be described as follows: The OA stage is the defect compaction stage. At the beginning of loading, the curve first rises vertically and then bends, which indicates that the specimen can resist certain deformation in the initial stage.

As the load increases, the defects existing in the specimen are compressed. The length of the curve for this stage depends on the internal microstructure in the specimen. The less the internal micro-structures in the specimen are, the shorter the stage is, and the more the internal defects are, the longer the stage is. The AB stage is the linear elastic stage, and the stress shows obvious linear relationship with the strain. At this stage, a small number of micro-cracks are initiated inside the rock specimen, and these micro-cracks have a negative impact on the mechanical properties of the rock. The BC stage is the macroscopic failure stage, in which the slope of the stress-strain curve gradually increases, and the deformation rate of the specimen becomes faster and faster. The gradual degradation of rock stiffness causes the appearance of macroscopic cracks and a large increase in strain. The failure of the sandstone specimen shows obvious brittleness. Different from the previous works (Cheng *et al.* 2021, Zhao *et al.* 2019), the loading rates of uniaxial compression test is kept constant to study the relationship between the mechanical behavior of the specimen and the angle of the prefabricated crack. From Figs. 9(a)-9(c) and Table 2, we can conclude that there is a relationship between the peak stress and the α, β angles. It is found that in each group, the peak axial stress of each specimen increases with the increase of the corresponding α and β angles. For example, the axial stress peaks of Nos. specimens 4-6 in Fig. 9(b) are increased from 25.28 MPa to 28.26 MPa, and the angles are increased from (45°, 30°) to (60°, 45°). This shows that the increase of prefabricated cracks within a certain range lead

Table 2 Experimental data

Rock type	Specimen	The angle α of pre-existing cracks(°)	The angle β of pre-existing cracks(°)	Peak force (KN)	Compression strength (MPa)	Young's modulus (MPa)
sandstone	Intact	/	/	58.98	30.04	8141.76
	1	30	0	43.44	22.12	3399.51
	2	60	0	48.13	24.51	3714.77
	3	90	0	52.23	26.60	3962.48
	4	45	30	49.64	25.28	4470.90
	5	60	30	52.37	26.67	4500.26
	6	60	45	55.49	28.26	5019.95
	7	30	90	44.88	22.86	3324.42
	8	45	90	48.03	24.46	3498.58
	9	60	90	55.33	28.18	3608.79
The average value of pre-cracked specimens				49.95	25.44	3944.41

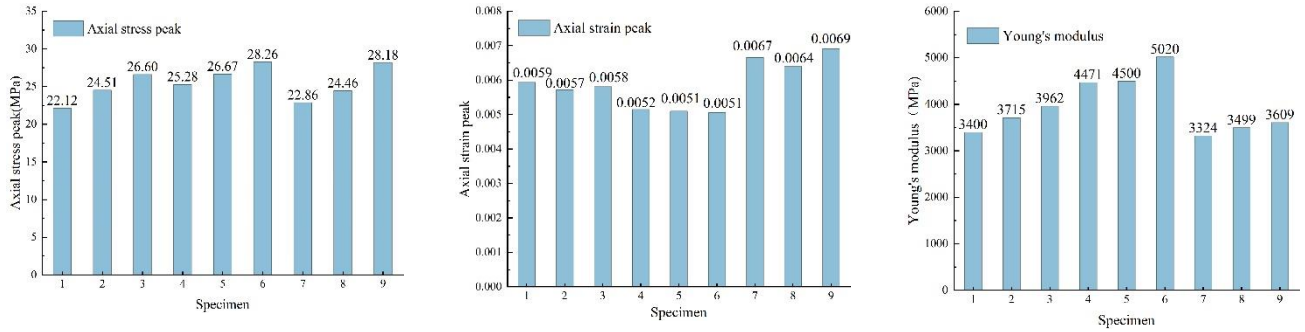

(a) Axial peak stress (b) Axial peak strain (c) Young's modulus

Fig. 10 Comparison of experimental data of specimens

to the increase of the peak axial stress. Fig. 10 shows the comparisons among the axial peak stress, axial peak strain, and Young's modulus of the specimens in the compression test. As shown in Fig. 10, from No.1 to No.6 specimen, the angle of the pre-existing cracks increased from (0°,30°) to (60°,45°), and the value of the peak stress changed from 22.12 MPa to 28.26 MPa. The maximum value of peak stress is 1.28 times larger than the minimum one. It can be concluded that the angle of the pre- existing cracks will affect the strength of the specimen. In Figs. 10(a) and 10(b), with the increase of the angle, the axial peak strain of specimens No.1-6 shows a downward trend, from 0.0059 to 0.0051. The Young's modulus shows an upward trend, from 3400 MPa to 5020 MPa. The angles of the pre-existing cracks of No.4-6 specimens are (45°, 30°), (60°, 30°), (60°, 45°), respectively. The angle of the pre-existing racks in second group is the closest to each other among the three groups. The Young's moduli of No.4-6 specimens are 4471 MPa, 4500 MPa, and 5020 MPa, respectively, which are larger than those of other specimens. This phenomenon shows that the more similar the angles of pre-existing cracks are, the larger the Young's moduli of the rock specimens are. The axial peak strain of the specimens in third group is larger than that in the first two groups, and the Young's modulus of the specimens in third group is also smaller than that of the first two groups. The angles of the pre-existing cracks have a great influence on the mechanical parameters of the specimens, which also makes the mechanical performance of the specimens in the third group different from that of the specimens in the first two groups. It can be found from Table 2 that the peak stress and the Young's modulus of all pre-cracked specimens are smaller than those of intact specimens. The uniaxial compressive strength of the intact specimen is 1.18 times higher than the average uniaxial compressive strength of the pre-cracked specimen, and the Young's modulus is 2.06 times higher than the average Young's modulus of the pre-cracked specimen, which proves that the pre-existing crack significantly reduces the strength of rock.

4.2 Crack growth pattern

Crack evolution begins with cracks that form around the edges of the concretions and then merges with cracks that propagate in the upper left and lower right corners of the sample (Chen *et al.* 2020). In this paper, the failure morphology of the cracks in the 9 specimens after compression is shown in Fig. 11. The rock failure process contai initiation, propagation, and connection of various cracks in ns the the rock. The distribution of primordial defects and pre-existing cracks affects the heterogeneity of

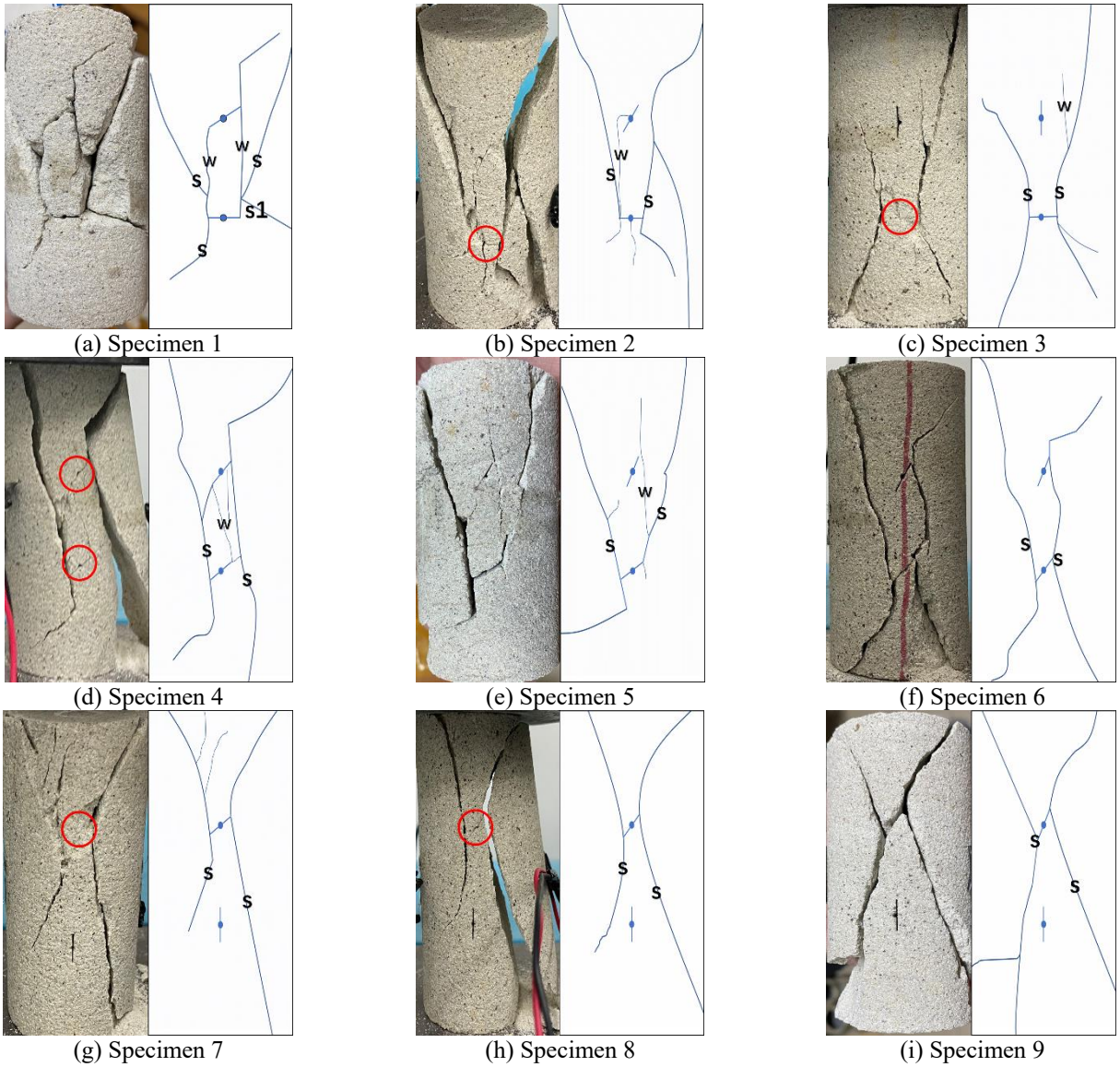

(a) Specimen 1 (b) Specimen 2 (c) Specimen 3

(d) Specimen 4 (e) Specimen 5 (f) Specimen 6

(g) Specimen 7 (h) Specimen 8 (i) Specimen 9

Fig. 11 The morphology of cracks in specimen compression

rocks. The heterogeneity profoundly affects the morphology of the cracks in the rock. The bifurcation of the cracks decreases with the decrease of primordial defects while the cracks are expanding at the tips of the pre-existing cracks according to the failure criterion. In other words, the failure morphology of the cracks will be irregular, and the bifurcation will increases if the primordial defects are rich in the crack development zone. The influence of primordial defects on the mechanical behavior of rock is dependent on the change and transfer of stress. The distribution of the stress concentration area is related to the shape, distribution, quantity, and size of the primordial defects in the rock.

Rock is a combination of solid minerals. During the rock compression test, due to the interactions between different components, the stress situation in the local area become complex in the rock and lead to the diversity of the crack patterns.

Under the uniaxial compression test, 9 rock specimens prefabricated with double-cracks in different angles are prepared to study the influence of crack inclination on the fracture patterns of rock specimens. In Fig. 11, “S” represents secondary cracks, “S1” represents secondary coplanar cracks, and “W” represents wing cracks. From Fig. 11, we can know that the failure of each specimen containing the prefabricated crack is caused by the initiation and propagation of cracks, resulting in a penetrating failure surface regardless of the angle of the prefabricated crack.

The cracks produced by compression propagate in a bending path. The propagation asymptote is far away from the axial loading direction. The wing crack “W” and secondary crack “S” are produced in Nos. 1-5 specimens. The secondary coplanar crack “S1” is only produced in No.1 specimen. There are only secondary cracks produced in Nos. 6-9 Specimens. The spatial shape of the wing crack shows a stable expansion along the curve path towards the direction of the maximum principal stress, and the spatial shape of the secondary crack shows undulation and bending. The reason may be that the secondary crack is

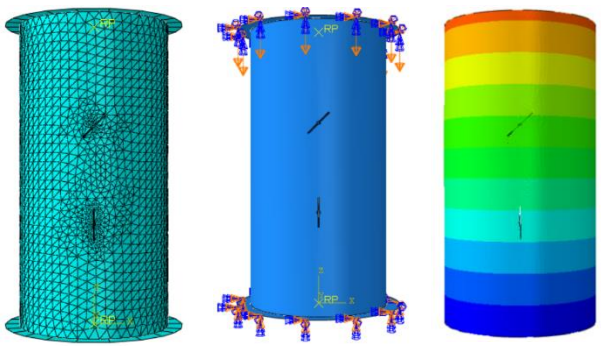

(a) The rock model after mesh (b) Constraints and displacement conditions (c) Field variable distribution

Fig. 12 The Numerical rock model

affected by the friction force, therefore there is a shear slip phenomenon during its expansion.

The degree of fragmentation of No. 1 and No. 2 specimens is the highest among the nine specimens, indicating that when the angles of the prefabricated crack are (0°, 30°) and (0°, 60°), the rock specimen is the most unstable and the compression failure is the most complete. Nos. 4-5 specimens produced wing cracks under compression. However, there are no wing crack in Nos. 6-9 specimens, which indicates that with the increase of the angle of the prefabricated cracks, the crack form changes from wing cracks to only secondary cracks. The crack propagation paths of Nos. 7-9 are similar to each other. A secondary crack is generated from both sides of the upper prefabricated crack. Both the angle β of the Nos. 7-9 specimens and the angle α of the No.3 specimen are equal to 90 °, and their crack propagation paths show a state of up and down reversal, which indicates that the cracks do not initiate from the prefabricated crack with an angle of 90°, the position of the 90° prefabricated crack will also affect the final crack propagation path of the rock. In addition, after the failure of the specimen, it can be found that some prefabricated cracks change from open type to closed type (the cracks in No. 2, 3, 4, 7, and 8, which are marked with red circles in Fig. 11). This leads to the development of the original crack and decrease of stress concentration.

5. Numerical simulation

5.1 Establishment of a numerical model

Based on the cohesive element method, the failure process of the rock specimen with pre-existing cracks is explored. A cylindrical rock model is created in Abaqus, the size of the model is 50 mm × 50 mm × 100 mm, and the type of the element is C3D10. The distribution and angle of pre-existing cracks in the model are consistent with those in the No.8 specimen. Rigid planes are added to the end faces of the numerical model. The contact between the rigid plane and the numerical model is hard and frictionless. One of the end faces is fixed. The movement rate of the displacement in the other end face is set to 2 mm/min, which is consistent

Fig. 13 The binarization of CT scan data

with that in the test. Through rigid plate, the realistic displacement loading boundary conditions can be reached. The finite element model and boundary condition are shown in Figs. 12(a) and 12(b).

The binary image of the CT data is shown in Fig. 13. To distinguish the matrix from the pores in the CT data, binarization is employed to uniformly process the gray value of the pixels on the image with an appropriate threshold. The binary image presents two distinct colors, i.e., black or white. After the multi-level values of the image pixels are converted, only the pixels in values of 0 or 255 left. Then, if the value is 255, it means that the pixel is judged as a specific object and appears to be black. If the value is 0, the pixel is excluded from the object area, indicating a non-specific object and appears to be white.

The black area represents the rock matrix, and the white area represents the pores or the primordial defects. Due to the continuous geological movement, natural rocks show complex heterogeneity and discontinuity. The shape, size, and distribution of primordial defects in the rock have a significant influence on the mechanical properties of the rock.

After binarization, porosity can be obtained by the percentage of white pixels in the CT data. Young's modulus of the rock material is assigned according to porosity in subsequent numerical modelling. To study the effect of pore structure on rock mechanical properties, Zhou and Xiao (2017) studied the relationship between porosity and fractal dimension by reconstructing a numerical rock model. It is found that the strength, Young's modulus, and porosity of sandstone are closely related to each other. After analysis of the Maxwell-type model (Lomax *et al.* 2002), the self-consistent model (Budiansky and O'Connell 1976), the differential scheme model (Hashin 1988), the exponential model (Pabst and Gregorová 2004) for predicting the relationship between porosity and Young's modulus, we adopt the exponential model in this paper. In addition, the work of Pabst *et al.* (2013) also confirmed that the exponential model is the best model to describe the relationship between porosity and Young's modulus. The exponential model employed in this paper can be expressed as follows

$$E_r = \exp\left(\frac{-2p}{1-p}\right), E_r = \frac{E}{E_o} \tag{8}$$

Table 3 Parameters of porosity, Young's modulus, and Field variables

Field	10	20	30	40	50	60	70	80	90
p	0.157	0.136	0.136	0.199	0.162	0.190	0.181	0.160	0.203
Young's Modulus (MPa)	3784.31	4008.94	4008.94	3341.65	3731.12	3435.65	3530.15	3752.38	3300.03

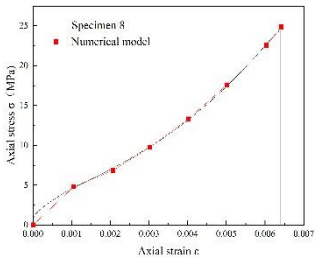

Fig. 14 Comparison of experimental data and numerical results

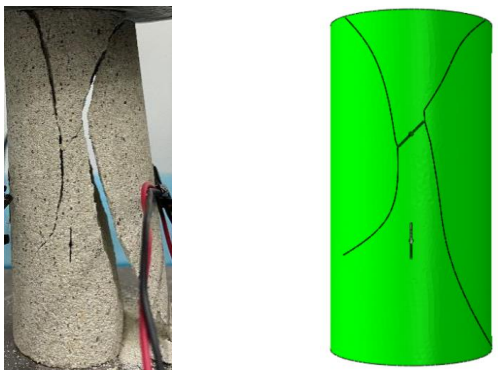

(a) Experimental results (b) Numerical results

Fig. 15 The path of crack propagation

where p is the porosity, E_r is the relative Young's modulus, E is Young's modulus of the porous material, and E_0 is Young's modulus of the intact rock material without pores. The average value of porosity of CT data is calculated as p=0.184.

The exponential model presents the relationship between Young's modulus and porosity. According to this model, Young's moduli for different sections with different heights in the numerical rock model can be calculated by the porosity obtained from the CT data at corresponding positions of rock specimens. Then, the corresponding Young's moduli are assigned to different sections of the numerical rock model, which indicates the anisotropy of the rock. However, the corresponding material model is not provided in Abaqus and needs to be implemented with other tools. Abaqus provides the field variables method to define material properties. The field variable in Abaqus is an environment variable for defining material parameters. The calculation of the field variable depends on the spatial coordinates. The Z-direction of the numerical model in this paper is set to be the vertical direction, and the value of each node in the Z direction, or the height, is set as a unique field variable so that Young's modulus can be assigned according to the spatial position of the corresponding section. The CT test is carried out from one end to the other end with the height, the Young's modulus is assigned to the corresponding section of the model to consider the anisotropy. The Young's moduli for different sections of the model can be calculated by the exponential model according to the porosity. The porosity, Young's modulus, and field variable parameters for each section are listed in Table 3. The corresponding Young's modulus for the field variable is calculated by interpolation of the Young's moduli of the two adjacent sections. The field variable distribution is shown in Fig. 12(c).

5.2 Modelling results

The comparison between the experimental data and the numerical results is shown in Fig. 14. The stress-strain curve of the experiment is almost consistent with that of the numerical model. The numerical simulation methodsimplifies the material properties during the numerical analysis, and the initial loading speed in numerical modelling is not exactly the same as the experimental loading speed, which results in a difference between the test and the numerical simulation at the initial stage. The peak strength of the rock model is about 24 MPa, which is similar to the experimental data. It can be found that the path of crack propagation in the numerical model is consistent with that in the experiment as shown in Fig. 15, which verifies the cohesive element method and field variables method.

By using finite element software, it is possible to clearly visualize how the mechanical state of the study object changes from one moment to another (Chong *et al.* 2017, Dehghanbanadaki *et al.* 2020, Jaiswal and Kumar 2022). The stress contour of the rock model failure in this paper is shown in Fig. 16. The stress is changed from small to large with the change of color from blue to red. The red region, which means stress concentration, appears near the tip of the pre-existing crack in time step 1 as shown in Fig. 16(a), and new cracks initiate from the tip of the pre-existing crack. The color of the region near the crack changes from red to blue, showing obvious stress release. In time step 2 as shown in Fig. 16(b), with the increase of load, the cracks gradually propagate towards the end of the specimen, and the direction of propagation is indicated by the stress contour in time step 1. At the same time, it can be found that there is a significant stress difference on both sides of the extended crack, indicating that tensile failure occurs. In the compression of the numerical rock model, the crack propagates from the tip of the pre-existing crack to the end face of the numerical model as shown in time step 3 as shown in Fig. 16(c). The final numerical result is shown in Fig. 16(d) in time step 4, and one of the pre-existing cracks

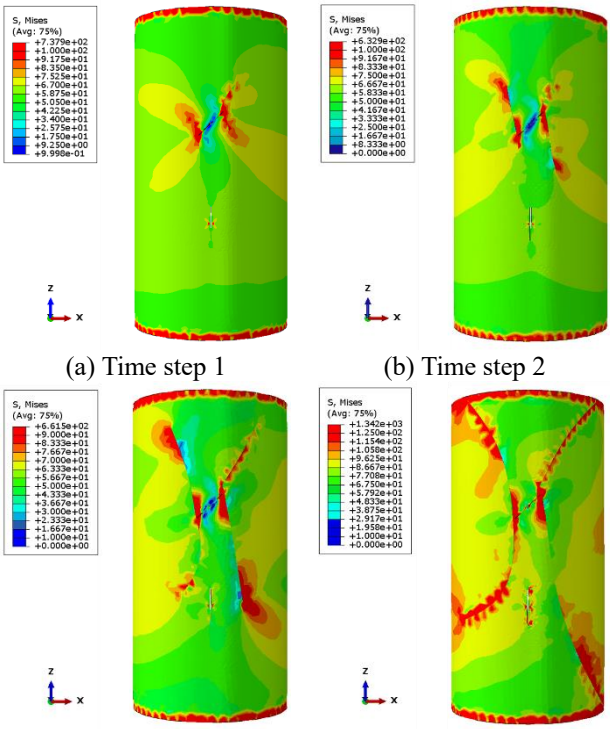

(a) Time step 1 (b) Time step 2

(c) Time step 3 (d) Time step 4

Fig. 16 Stress cloud picture of Numerical rock model

in the numerical model is closed. In addition, the change of the other pre-existing crack is not obvious during the numerical process, and no new cracks are generated from both ends of the pre-existing crack. By analyzing the stress graph or contour of No. 8 specimen in Fig. 16, combined with the fracture patterns of No. 3, 7, 8 and 9 specimens in Fig. 11, it can be found that no matter where the prefabricated crack is, when the α or β angle is 90°, the stress concentration does not generate at the end of the prefabricated crack, therefore no crack initiates and propagates from the end of the prefabricated crack. This indicates that if the angle of the prefabricated crack is consistent with the direction of the compression stress, the stress concentration will not generate at the end of the prefabricated crack. These numerical results described above are consistent with the experimental results.

6. Conclusions

In this paper, the longitudinal anisotropy of rock is considered in the modeling. The porosity of rock specimens was calculated based on CT data, and the relationship between porosity and Young's modulus was studied. The field variable method is used to determine the material properties of the numerical rock model. The initiation and propagation of cracks in rock specimens with prefabricated cracks were studied by cohesive element method. The numerical results are consistent with the experimental results, which verifies the cohesion element method and field variable method. Rock is an anisotropic medium. In practice, it is anisotropic in all directions. By establishing a three-dimensional reconstructed rock model to characterize the pore distribution, the anisotropy of rock in different directions can be considered in our future work.

The cohesive element method in this paper can be used to predict rock engineering disasters such as rock collapse, landslide and ground collapse caused by crack propagation, which provides a powerful tool for reasonable selection of engineering technology. In this paper, the influence of the angle of the prefabricated crack on mechanical properties and fracture property of rock under compression are studied. The porosity of rock was obtained by CT scanning, and the relationship between porosity and Young 's modulus was established. Through the field variable method, the Young's modulus which changes with the spatial position is assigned to the rock model. Finally, based on the cohesive element method, the numerical analysis of the failure of the rock model with prefabricated cracks has been done. The conclusions are drawn as follows:

(1) The prefabricated cracks reduce the mechanical properties of rock, the closer to each other the angles of prefabricated cracks is, the greater the Young 's modulus of rock samples are.

(2) In the compression test, the failure process of each specimen with prefabricated cracks is formed by the initial crack initiation and propagation. The cracks expand in the bending path, and the expansion asymptote is far away from the axial loading direction.

(3) Numerical results verify the effectiveness of the cohesive element method in this paper. The method adopted in this paper reflects the rock microstructure in the numerical model.

Acknowledgments

The research was financially supported by The National Natural Science Foundation of China (Grant Nos. 51908067, 51878074).

References

Altindag, R. and Güney, A. (2006), "ISRM suggested method for determining the shore hardness value for rock", *Int. J. Rock. Mech. Min.*, **43**(1), 19-22. https://doi.org/10.1016/j.ijrmms.2005.04.004.

Barenblatt, G.I. (1962), "The mathematical theory of equilibrium cracks in brittle fracture", *Adv. Applmech.*, **7**, 55-129. https://doi.org/10.1016/S0065-2156(08)70121-2.

Budiansky, B. and O'Connell R.J. (1976), "Elastic moduli of a cracked solid", *Int. J. Solids. Struct.*, **12**(2), 81-97. https://doi.org/10.1016/0020-7683(76)90044-5.

Cascio, M.L., Milazzo, A. and Benedetti, I. (2021), "A hybrid virtual–boundary element formulation for heterogeneous materials", *Int. J. Mech. Sci.*, **199**, 106404. https://doi.org/10.1016/j.ijmecsci.2021.106404.

Cheng, Y., Song, Z.S., Song, W.X., Li, S.G., Yang, T.T., Zhang, Z.K., Wang, T. and Wang, K.S. (2021), "Strain performance and fracture response characteristics of hard rock under cyclic disturbance loading", *Geomech. Eng.*, **26**(6), 551-563. https://doi.org/10.12989/gae.2021.26.6.551

Chen, S.J., Ren, M.Z., Wang, F., Yin, D.W. and Chen, D.H. (2020), "Mechanical properties and failure mechanisms of sandstone

with pyrite concretions under uniaxial compression", *Geomech. Eng*., **22**(5), 385-396. https://doi.org/10.12989/gae.2020.22.5.385.

Chong, S.H., Cho, G.C., Hong, E.S. and Lee, S.W. (2017), "Numerical study of anomaly detection under rail track using a time-variant moving train load", *Geomech. Eng*., **13**(1), 161-171. https://doi.org/10.12989/gae.2017.13.1.161.

Dehghanbanadaki, A., Motamedi, S. and Ahmad, K (2020), "FEM-based modelling of stabilized fibrous peat by end-bearing cement deep mixing columns", *Geomech. Eng*., **20**(1), 75-86. https://doi.org/10.12989/gae.2020.20.1.075.

Dugdale, D.S. (1960), "Yielding of steel sheets containing slits", *J. Mech. Phys. Solids*., **8**(2), 100-104. https://doi.org/10.1016/0022-5096(60)90013-2.

Fakhimi, A. and Alavi Gharahbagh, E. (2011), "Discrete element analysis of the effect of pore size and pore distribution on the mechanical behavior of rock", *Int. J. Rock. Mech. Min*., **48**(1), 77-85. https://doi.org/10.1016/j.ijrmms.2010.08.007.

Galindo, R., Andres, J.L., Lara, A., Xu, B., Cao, Z.G. and Cai, Y.Q. (2021), "Theoretical model for the shear strength of rock discontinuities with non-associated flow laws", *Geomech. Eng*., **24**(4), 307-321. https://doi.org/10.12989/gae.2021.24.4.307.

Hashin, Z. (1988), "The differential scheme and its application to cracked materials", *J. Mech. Phys. Solids*., **36**(6), 719-734. https://doi.org/10.1016/0022-5096(88)90005-1.

Hillerborg, A., Modéer, M. and Eersson P.E. (1976), "Analysis of crack formation and crack growth in concrete by means of fracture mechanics and finite elements", *Cement. Concrete. Res*., **6**(6), 773-781. https://doi.org/10.1016/0008-8846(76)90007-7.

Hoover, C.G. and Bažant, Z.P. (2014), "Cohesive crack, size effect, crack band and work-of-fracture models compared to comprehensive concrete fracture tests", *Int. J. Fracture*., **187**, 133-143. https://doi.org/10.1007/s10704-013-9926-0.

Hong, S.K., Oh, D.K., Kong, S.M. and Lee, Y.J. (2020), "Investigation of divergence tunnel excavation according to horizontal offsets between tunnels", *Geomech. Eng*., **21**(2), 111-122. https://doi.org/10.12989/gae.2020.21.2.111.

Jaiswal, A. and Kumar, R. (2022), "Finite element analysis of granular column for various encasement conditions subjected to shear load", *Geomech. Eng*., **29**(6), 645-655. https://doi.org/10.12989/gae.2022.29.6.645.

Jiang, H.X. and Meng, D.G. (2018), "3D numerical modelling of rock fracture with a hybrid finite and cohesive element method", *Eng. Fract. Mech*., **199**, 280-293. https://doi.org/10.1016/j.engfracmech.2018.05.037.

Lee, H.W. and Jeon, S.W. (2011), "An experimental and numerical study of fracture coalescence in pre-cracked specimens under uniaxial compression", *Int. J. Solids. Struct*., **48**(6), 979-999. https://doi.org/10.1016/j.ijsolstr.2010.12.001.

Leonel, E.D. and Venturini, W.S. (2011), "Multiple random crack propagation using a boundary element formulation", *Eng. Fract. Mech*., **78**(6), 1077-1090. https://doi.org/10.1016/j.engfracmech.2010.11.012.

Li, H.Q. and Wong, L.N.Y. (2012), "Influence of flaw inclination angle and loading condition on crack initiation and propagation", *Int. J. Solids. Struct*., **49**(18), 2482-2499. https://doi.org/10.1016/j.ijsolstr.2012.05.012.

Liu, X.R., Liu, D.S., Xiong, F., Han, Y.F., Liu, R.H., Meng, Q.J., Zhong, Z.L., Chen, Q.,Weng, C.X. and Liu, W.W. (2022), "Experimental and numerical study on the stability of slurry shield tunneling in circular-gravel layer with different cover-span ratios", *Geomech. Eng*., **28**(3), 265-281. https://doi.org/10.12989/gae.2022.28.3.265.

Lomax, H., Pulliam, T.H., Zingg, D.W. and Kowalewski, T.A. (2002), "Fundamentals of computational fluid dynamics", *Appl. Mech. Rev*., **55**(4), B61. https://doi.org/10.1115/1.1483340.

Nguyen, N.H.T., Bui, H.H., Nguyen, G.D. and Kodikara, J. (2017), "A cohesive damage-plasticity model for DEM and its application for numerical investigation of soft rock fracture properties", *Int. J. Plasticity*., **98**, 175-196. https://doi.org/10.1016/j.ijplas.2017.07.008.

Pabst, W. and Gregorová, E. (2004), "Mooney-type relation for the porosity dependence of the effective tensile modulus of ceramics", *J. Mater. Sci*., **39**, 3213-3215. https://doi.org/10.1023/B:JMSC.0000025863.55408.c9.

Pabst, W., Gregorová, E. and Černý, M. (2013), "Isothermal and adiabatic Young's moduli of alumina and zirconia ceramics at elevated temperatures", *J. Eur. Ceram. Soc*., **33**(15-16), 3085-3093. https://doi.org/10.1016/j.jeurceramsoc.2013.06.012.

Pan, C., Li, X., He, L. and Li, J.C. (2021), "Study on the effect of micro-geometric heterogeneity on mechanical properties of brittle rock using a grain-based discrete element method coupling with the cohesive zone model", *Int. J. Rock. Mech. Min*., **140**, 104680. https://doi.org/10.1016/j.ijrmms.2021.104680.

Pradhan, S.P. and Siddique, T. (2020), "Stability assessment of landslide-prone road cut rock slopes in Himalayan terrain: A finite element method based approach", *J. Rock. Mech. Geotech*., **12**(1), 59-73. https://doi.org/10.1016/j.jrmge.2018.12.018.

Scholtès, L. and Donzé, F.V. (2012), "Modelling progressive failure in fractured rock masses using a 3D discrete element method", *Int. J. Rock. Mech. Min*., **52**, 18-30. https://doi.org/10.1016/j.ijrmms.2012.02.009.

Song, S.H., Paulino, G.H. and Buttlar, W.G. (2006), "A bilinear cohesive zone model tailored for fracture of asphalt concrete considering viscoelastic bulk material", *Eng. Fract. Mech*., **73**(18), 2829-2848. https://doi.org/10.1016/j.engfracmech.2006.04.030.

Su, X.T., Yang, Z.J. and Liu, G.H. (2010a), "Finite element modelling of complex 3D static and dynamic crack propagation by embedding cohesive elements in abaqus", *Acta. Mech. Solida. Sin*., **23**(3), 271-282. https://doi.org/10.1016/S0894-9166(10)60030-4.

Su, X.T., Yang, Z.J. and Liu, G.H. (2010b), "Monte Carlo simulation of complex cohesive fracture in random heterogeneous quasi-brittle materials: A 3D study", *Int. J. Solids. Struct*., **47**(17), 2336-2345. https://doi.org/10.1016/j.ijsolstr.2010.04.031.

Unger, J.F., Eckardt, S. and Könke, C. (2007), "Modelling of cohesive crack growth in concrete structures with the extended finite element method", *Comput. Method. Appl. M*., **196**(41-44), 4087-4100. https://doi.org/10.1016/j.cma.2007.03.023.

Wu, K., Shao, Z.S., Qin, S. and Zhao, N.N. (2019), "Mechanical analysis of tunnels supported by yieldable steel ribs in rheological rocks", *Geomech. Eng*., **19**(1), 61-70. https://doi.org/10.12989/gae.2019.19.1.061.

Wu, Z.J., Xu, X.Y., Liu, Q.S. and Yang, Y.T. (2018), "A zero-thickness cohesive element-based numerical manifold method for rock mechanical behavior with micro-Voronoi grains", *Eng. Anal. Bound. Elem.,* **96**, 94-108. https://doi.org/10.1016/j.enganabound.2018.08.005

Xie, Y.S., Cao, P., Liu, J. and Dong, L.W. (2016), "Influence of crack surface friction on crack initiation and propagation: A numerical investigation based on extended finite element method", *Comput. Geotech*., **74**, 1-14. https://doi.org/10.1016/j.compgeo.2015.12.013.

Yang, S.Q., Tian, W.L., Huang, Y.H., Ma, Z.G., Fan, L.F. and Wu, Z.J. (2018), "Experimental and discrete element modeling on cracking behavior of sandstone containing a single oval flaw under uniaxial compression", *Eng. Fract. Mech*., **194**, 154-174. https://doi.org/10.1016/j.engfracmech.2018.03.003.

Zhao, B.Y., Huang, T.Z., Liu, D.Y., Liu, Y., Wang, X.P., Liu, S.

and Yu, G.B. (2019), "Study on the mechanical properties test and constitutive model of rock salt", *Geomech. Eng*., **18**(3), 291-298. https://doi.org/10.12989/gae.2019.18.3.291.

Zhou, W., Tang, L.W., Liu, X.H., Ma, G. and Chen, M.X. (2016), "Mesoscopic simulation of the dynamic tensile behaviour of concrete based on a rate-dependent cohesive model", *Int. J. Impact. Eng*., **95**, 165-175. https://doi.org/10.1016/j.ijimpeng.2016.05.003

Zhou, X.P. and Xiao, N. (2017), "A novel 3D geometrical reconstruction model for porous rocks", *Eng. Geol*., **228,** 371-384. https://doi.org/10.1016/j.enggeo.2017.08.021.

GC